ISSN 1674-1056
http://cpb.iphy.ac.cn
http://iopscience.iop.org/cpb
中国物理 B
Chinese Physics
中国物理 Chinese Physics B

Scanning transmission electron microscopy:A review of high angle annular dark field and annular bright field imaging and applications in lithium-ion batteries

Yu-Xin Tong(仝毓昕), Qing-Hua Zhang(张庆华), Lin Gu(谷林)
Citation: Chin. Phys. B . 2018, 27(6): 066107. **doi:** 10.1088/1674-1056/27/6/066107

Journal homepage: http://cpb.iphy.ac.cn; http://iopscience.iop.org/cpb

What follows is a list of articles you may be interested in

Polycrystalline cubic boron nitride prepared with cubic-hexagonal boron nitride under high pressure and high temperature

Ming Yang(杨鸣), Zi-Li Kou(寇自力), Teng Liu(刘腾), Jing-Rui Lu(卢景瑞), Fang-Ming Liu(刘方明), Yin-Juan Liu(刘银娟), Lei Qi(戚磊), Wei Ding(丁未), Hong-Xia Gong(龚红霞), Xiao-Lin Ni(倪小林), Duan-Wei He(贺端威)
Chin. Phys. B . 2018, 27(5): 056105. **doi:** 10.1088/1674-1056/27/5/056105

Influence of Tb on easy magnetization direction and magnetostriction of ferromagnetic Laves phase $GdFe_2$ compounds

Adil Murtaza, Sen Yang(杨森), Chao Zhou(周超), Xiaoping Song(宋晓平)
Chin. Phys. B . 2016, 25(9): 096107. **doi:** 10.1088/1674-1056/25/9/096107

FT-Raman spectroscopy study of solvent-in-salt electrolytes

Liumin Suo(索鎏敏), Zheng Fang(方铮), Yong-Sheng Hu(胡勇胜), Liquan Chen(陈立泉)
Chin. Phys. B . 2016, 25(1): 016101. **doi:** 10.1088/1674-1056/25/1/016101

High-pressure effect on inverse spinel $LiCuVO_4$: X-ray diffraction and Raman scattering

Liang Heng-Nan, Ma Chun-Li, Du Fei, Cui Qi-Liang, Zou Guang-Tian
Chin. Phys. B . 2013, 22(1): 016103. **doi:** 10.1088/1674-1056/22/1/016103

Pressure-induced structural transition and thermodynamic properties of RhN_2 and effect of metallic bonding on its hardness

Liu Jun, Kuang Xiao-Yu, Wang Zhen-Hua, Huang Xiao-Fen
Chin. Phys. B . 2012, 21(8): 086103. **doi:** 10.1088/1674-1056/21/8/086103

TOPICAL REVIEW — Electron microscopy methods for the emergent materials and life sciences

Scanning transmission electron microscopy: A review of high angle annular dark field and annular bright field imaging and applications in lithium-ion batteries*

Yu-Xin Tong(仝毓昕)[1,2], Qing-Hua Zhang(张庆华)[1,†], and Lin Gu(谷林)[1,2,‡]

[1] *Beijing National Laboratory for Condensed Matter Physics, Institute of Physics, Chinese Academy of Sciences, Beijing* 100190, *China*
[2] *School of Physical Sciences, University of Chinese Academy of Sciences, Beijing* 100190, *China*

(Received 15 November 2017; revised manuscript received 21 December 2017; published online 30 May 2018)

Scanning transmission electron microscopy (STEM) has been shown as powerful tools for material characterization, especially after the appearance of aberration-corrector which greatly enhances the resolution of STEM. High angle annular dark field (HAADF) and annular bright field (ABF) imaging of the aberration-corrected STEM are widely used due to their high-resolution capabilities and easily interpretable image contrasts. However, HAADF mode of the STEM is still limited in detecting light elements due to the weak electron-scattering power. ABF mode of the STEM could detect light and heavy elements simultaneously, providing unprecedented opportunities for probing unknown structures of materials. Atomic-level structure investigation of materials has been achieved by means of these imaging modes, which is invaluable in many fields for either improving properties of materials or developing new materials. This paper aims to provide a introduction of HAADF and ABF imaging techniques and reviews their applications in characterization of cathode materials, study of electrochemical reaction mechanisms, and exploring the effective design of lithium-ion batteries (LIBs). The future prospects of the STEM are also discussed.

Keywords: scanning transmission electron microscopy, high angle annular dark field, annular bright field, lithium-ion batteries

PACS: 61.50.Ks, 68.37.Ma, 82.45.Fk, 82.47.Aa **DOI:** 10.1088/1674-1056/27/6/066107

1. Introduction

To reveal the structural features of materials at multiple scales, various characterization techniques have been employed, including x-ray diffraction (XRD), neutron powder diffraction (NPD), x-ray absorption spectroscopy (XAS), and electron microscopy. XRD and NPD have been implemented in structural characterization to obtain the crystallographic information, such as structural features and lattice parameters. XAS has been widely applied to probe the evolution of the chemical environment and electronic structure. However, these techniques suffer from a few limitations due to their lower spatial resolutions.

Electron microscopy is a broad term that includes scanning electron microscopy (SEM), scanning tunneling microscopy (STM), transmission electron microscopy (TEM), and scanning transmission electron microscopy (STEM). SEM is mainly utilized for surface morphological characterization and STM is used to reveal the surface atomic and electronic structure. In particular, TEM and STEM have superior abilities in detecting the structure of materials with higher spatial resolution. In addition, they could provide information related to chemical composition and electronic structure. The aberration corrector, originally introduced by Scherzer,[1] makes it possible to achieve sub-angstrom resolution without using complex computation.[2–6] Given these prominent advantages, TEM and STEM have been used in many fields, such as physics, chemistry, material science, etc.[7,8] This review mainly focuses on HAADF and ABF imaging techniques and their applications in characterization of electrode materials for Li-ion batteries.

2. Brief history of TEM and STEM

Transmission electron microscopy was developed between the 1920s and 1930s. The French physicist De Broglie discovered the wave nature of electrons in 1924, proved by electron diffraction. The German scientist Busch suggested that an axisymmetrical magnetic field could focus the electron beam, providing the theoretical basis of TEM. Afterward, Knoll and Ruska used these concepts to successfully build the first TEM in 1934 Meanwhile, the theory of high-resolution transmission electron microscopy (HRTEM) was established and improved, promoting the field application of HRTEM. The atomic column of most crystals can be imaged by HRTEM. However, the intrinsic aberration of the lens, especially the

*Project supported by the National Basic Research Program of China (Grant No. 2014CB921002), the Strategic Priority Research Program of Chinese Academy of Sciences (Grant No. XDB07030200), and the National Natural Science Foundation of China (Grant Nos. 51522212, 51421002, and 51672307).

†Corresponding author. E-mail: zqh@iphy.ac.cn
‡Corresponding author. E-mail: l.gu@aphy.iphy.ac.cn

© 2018 Chinese Physical Society and IOP Publishing Ltd

spherical aberration, limits the resolution. The development of aberration corrector paved a great step forward for enhancing resolution.

Compared with TEM, a scanning focused incident electron beam rather than a static one is used in STEM. Moreover, an annular detector centering bright field is employed to collect scattered electrons in STEM. Pennycook *et al.* proposed high angle annular dark field (HAADF) imaging technique for STEM to obtain the atomic number (Z) contrast[9] and the direct visual interpretability of images and insensitivity to sample thickness were significantly advanced. The signal intensity of the atomic columns of HAADF was found almost proportional to $Z^{1.7}$.[9,10] However, when the light and heavy elements are present simultaneously, the weak signals from light elements are completely overwhelmed by the strong contrast issued from heavy elements.[10] Light elements have been shown to play important roles in advanced functional materials and devices. For example, the migration of Li atoms was found crucial in mechanisms of Li-ion batteries. Therefore, a great challenge is to make light and heavy elements visible simultaneously. This difficulty was solved in 2009 when Okunishi *et al*. reported an innovative imaging technique, called annular bright-field (ABF), where light and heavy elements in iron oxide, silicon nitride, and strontium titanate were simultaneously visualized.[11] After the first successful demonstration, increasing attention was paid to ABF imaging. Numerous experiments and theoretical studies confirmed that this imaging mode could visualize light and heavy elements simultaneously within a relative large range of specimen thickness and defocus value.[12–17] Using ABF imaging, numerous unknown structures have been discovered one after another. Nowadays, the advanced imaging techniques are utilized in various fields.

3. HAADF and ABF imaging theory

The electron beam would strongly interact with the electrons and nuclei of atoms in materials, encoding rich information about the samples. This could be focused by magnetic lenses to generate TEM and STEM imaging, and thus providing information with high spatial resolutions. To gain a better understanding of the imaging formation mechanism, the electron scattering inside samples will briefly be introduced. The scattering behavior of an electron beam inside crystals is of extremely high complexity, including elastic and inelastic scatterings. After the incident electron crashed with atoms in materials, the moving direction of the incident electron would change but the energy of the electron could keep the same, which is called elastic scattering. Both energy and direction of the incident electron would change after the collision, defining the inelastic scattering. Incoherent and elastically scattered electrons come into effect in HAADF images. BF images are mainly dominated by coherent and elastically scattered electrons. Early investigations showed that key features of ABF images are essentially determined by the coherent scattered electrons and influenced by thermal diffuse scattering (TDS). Although the contribution from TDS may be applicable to thicker specimens, the contrast between the different elements would not reverse. It is demonstrated that the effect of TDS could be neglected during ABF imaging of light elements.[13]

3.1. HAADF imaging theory

A low angle annular bright field (LABF) detector was initially installed in the STEM for sufficient collection of efficiency, where diffraction contrast made images pretty uninterpretable. Afterward, an HAADF detector was designed to obtain easy interpretation and higher resolution images by avoiding the impact of the Bragg scattering electrons. These electrons scattered in fairly large angles are incoherent and elastic, reflecting both the massive and thickness contrast. A schematic representation of ray diagram of HAADF and ABF is shown in Fig. 1. Based on the Rutherford scattering formula and by using several appropriate approximations, the contrast of HAADF images can simply be regarded as proportional to $Z^{1.7}$.[9,10] The images of HAADF were thus termed as the Z contrast images.

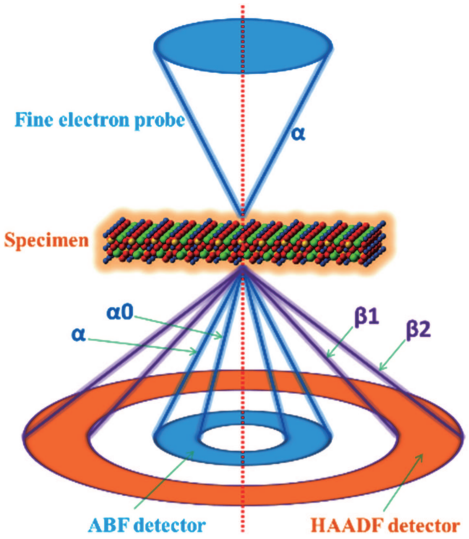


Fig. 1. (color online) Schematic representation of ray diagram of HAADF and ABF.

3.2. Dynamic theory of ABF

3.2.1. Optical configuration of ABF-STEM

A series of off-axial illumination over certain angles of the incident electron beam was applied in hollow-cone illumination (HCI) mode of TEM shown in Fig. 2(a). Some investigations suggested that HCI can remarkably enhance the resolution and abate signal-to-noise ratio[18–20] by removing the influence of chromatic aberration (Cc),[21] which is a considerable limitation in improving resolution. Based on reciprocity,[22] HCI can be realized by placing an annular detector within the bright-field region of the STEM, named as

ABF-STEM.[23] The detectors of ABF and ADF are schematically presented in Fig. 2(b).

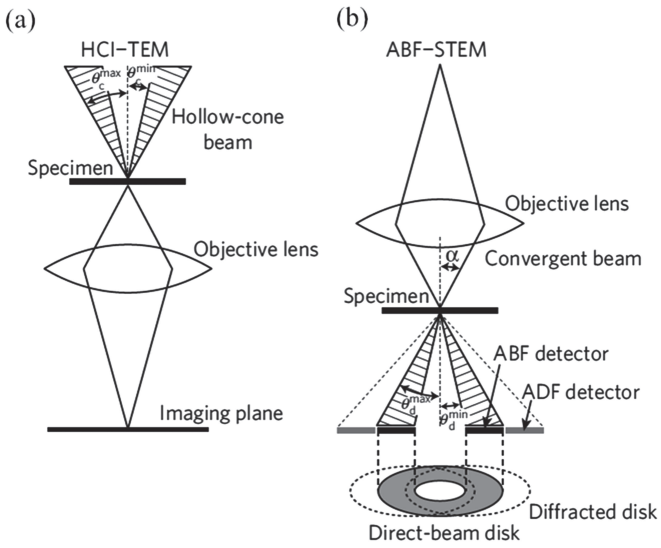


Fig. 2. The schematic representation of the ray diagram: (a) HCI-TEM and (b) ABF-STEM.[24]

3.2.2. S-state channeling model

The dynamic theory of ABF imaging in the STEM is mainly based on the s-state channeling model. Considering the electron scattering by Bloch wave method, some of the Bloch states would be strongly laid around the atomic columns, considered as a form of symmetry in electron orbitals of atomic theory. The s-state wave function is tightly bound to the atomic column, leading to insensitive intercolumn spacing.[25] When the electron probe of the STEM is directly placed above the signal atom column, the s-state wave function should become intensely excited. A qualitative analysis of imaging could be determined from the s-state behavior. However, some studies demonstrated that the s-state model is not applicable to the closely spaced column and fine electron probes.[25] The main idea of s-state channeling model is to divide the total wave function into s-state and grouped reminder contributions. When the incident electron probe is positioned above the single column, the wave function can be described as the following function of propagation distance z inside the specimen in reciprocal space:[12]

$$\Psi_0(q,z) \approx \alpha\Phi_{1s}(q)\exp\left[-i\pi\frac{E_{00}}{E_0}\frac{z}{\lambda}\right] + [A(q)-\alpha\Phi_{1s}(q)]\exp\left[-i\pi\lambda q^2 z\right], \quad (1)$$

where Φ_{1s} represents the s-state wave function, α is the s-state excitation amplitude, E_{00} is the s-state binding energy (negative).[17] E_0 is the accelerating voltage, A is the reciprocal space amplitude constant of the electron probe on the surface, λ is the electron wavelength, and q is the two-dimensional reciprocal vector.

The radial distribution of the scattered electrons would depend on the scattering angle β and the specimen thickness. $\alpha\Phi_{1s}$ and $A-\alpha\Phi_{1s}$ are functions of the scattering angle β and such relationships using the Si column test case are shown in Fig. 2. The value of $\alpha\Phi_{1s}$ would always be positive, the sign of $A-\alpha\Phi_{1s}$ varies with the scattering angle β, and the quantities of $\alpha\Phi_{1s}$ and $A-\alpha\Phi_{1s}$ are real. When z is equal to 0 Å, significant and constructive interference of both terms would induce the step function profile of the reciprocal space of the probe on the surface. In Fig. 3, three regions are roughly visible: (I) from $\beta=0$ mrad to 9.8 mrad ($A-\alpha\Phi_{1s}$ is negative), (II) from $\beta=9.8$ mrad to 22 mrad ($A-\alpha\Phi_{1s}$ is positive), and (III) from $\beta=22$ mrad outwards ($A-\alpha\Phi_{1s}$ is negative). In regions (I) and (III), because $A-\alpha\Phi_{1s}$ is negative, the value starts as maximal due to the relative phase shift in π between $A-\alpha\Phi_{1s}$ and $\alpha\Phi_{1s}$. The relative phase shift between the two terms varies with the propagation terms. Specifically, the relative phase shift becomes lower rather than higher than the initial value. The interference between the first and third values increases the net electron density. By contrast, the two terms start perfectly in phase with a relative phase of zero in the second region. The relative phase shift becomes superior to the initial value as the propagation distance changes. Therefore, the result of interference is the decrease in net electron density. In other words, the detector can be installed in a different range of the scattering angle to obtain contrast imaging.

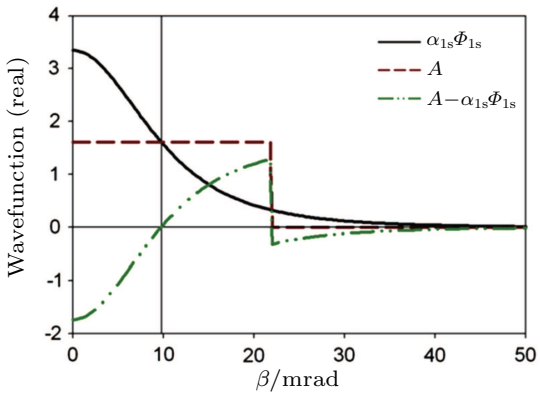


Fig. 3. (color online) Radial profiles of $\alpha\Phi_{1s}$, A, and $A-\alpha\Phi_{1s}$ assuming an aberration-free, 22 mrad aperture probe, and the Si column test specimen.[12]

Three cases with different relative locations of the electron probe and atomic column in the crystalline specimen are discussed.[17] I) The electron probe is positioned between two atomic columns. Given the features of the scattered electrons, the intensity distribution of the diffraction patterns is not seriously different from that in absence of the specimen. II) The electron probe is positioned on an atomic column of the light element. Some electrons are scattered into the dark field but most of the electrons are present in the center of the bright field. Because the total flux of the electrons in the diffraction

plane is the same for all probe positions, reduction in the electron densities in the outer region of the bright field occurs. The signal on ABF detector spanning the out of the bright field decreases. III) The electron probe is located in an atomic column of a heavy element. Most of the electrons are scattered out into the dark field owing to the strong scattering of the heavy atoms. The signal on the ABF detector decreases again.

Electron scattering which occurs as the atomically fine probe is often complicated, and considerable simplification is included in three situations. The s-state transversely bounded to the atomic column strongly interferes with the largely unscattered remaining states, inducing the net positive interference in the central portion and net negative interference in the outer portion.[12] Although the thickness of the specimen influences the details of interference, the discussion can provide a qualitative description of the interference tendency, where both light and heavy columns decrease the intensity in the outer region of the bright field, producing interpretable images, where both light and heavy atoms are visible simultaneously.

3.2.3. Defocus-thickness dependence of ABF images contrast

The simulated ABF defocus-thickness map of $SrTiO_3$ viewed along the [011] direction is shown in Fig. 4. A significant trait is that a band of images centered around zero defocus stretching out all considered thickness values, in which the form of ABF image did not change very much. Some reported experimental studies dealing with ABF imaging using aberration-correct STEM further demonstrated atomic columns with dark contrast over wide ranges of thicknesses (10 nm to 70 nm) and defocuses (−20 nm to +20 nm).[26] Thus, the ABF images showed the same feature that they were relatively insensitive to the thickness of the specimens.

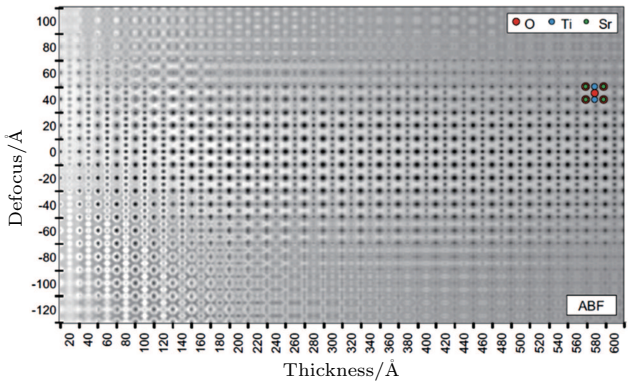


Fig. 4. (color online) Simulated ABF defocus-thickness map for $SrTiO_3$ viewed along the [011] direction.[12]

The simulated BF defocus-thicknesses map for $SrTiO_3$ viewed along the [011] direction was simulated. The contrast dramatically varies with the defocus value and thickness. Hence compared with usual bright field (BF) images, the robustness of visibility and interpretability of both light and heavy atom columns with respect to thickness in ABF images is better. Nevertheless, the fluctuation in ABF image contrast with thickness may lead to inability in distinguishing different kinds of elements. This could be prevented by recording HAADF images concurrently.

4. Applications in structural characterization of lithium ion battery cathode materials

Lithium-ion batteries (LIBs) were first commercialized in 1991 by Sony and currently used in many fields, such as portable electronics, electric vehicles, and smart grids. This is due to their high energy and power densities, as well as their superior cyclic stabilities and safety performances.[27–29] The cathode materials are vital components in the construction of LIBs, largely affecting the battery performances. The conventional cathode materials include olivine compounds $LiMPO_4$ (M = Fe, Mn, Ni, Co, etc.), layered compounds $LiMO_2$ (M = Co, Ni, Mn, etc.), and spinel compounds LiM_2O_4 (M = Mn, etc.). To improve the properties of LIBs and meet demands for emerging markets, understanding the structure and mechanism of the electrode materials is necessary. Although the atomic behavior of the Li ion primarily determines the electrochemical performances of LIBs, such information is hardly obtained by TEM technique due to the weak electron scattering of light atoms.[30] Considering the superior performances of ABF imaging in terms of simultaneous visibility of light and heavy atoms, ABF has been employed to reveal structural features of electrode materials and electrochemical reaction mechanism in LIBs.[31,32] In addition, the HAADF imaging technique has been widely used for investigating the structural evolution of electrode materials.

4.1. Olivine compound $LiFePO_4$

Since $LiFePO_4$ was first reported as a cathode material for LIBs,[33] it has increasingly attracted attention due to its low cost, safety performance and cyclic stability. Although the practical applications of $LiFePO_4$ in cathodes of LIBs have been realized for many years, several problems remained unsolved. For instance, the intrinsic low electronic conductivity[34–36] and poor ionic transport properties[37–40] were considered significant limitations in achieving high rate performances. Nanostructure[41–44] and surface coating[45–48] could overcome these drawbacks to some extent. The microscopic mechanism of structural evolution became essential in revealing the electrochemical reaction mechanisms and improving the properties of LIBs. An obvious voltage plateau appeared during the charge and discharge processes of LIBs based on $LiFePO_4$ cathodes. This suggested that a two-phase reaction in the $LiFePO_4$ cathode took place. Many models have been developed to explain the two-phase reaction

mechanism, including the core–shell model,[33] the shrinking model,[49] the mosaic model,[50] the new core–shell model,[51] and the domino-cascade model.[52] But all of these models failed to provide details on the structure of resulting two-phase interface region, essential to explain the two-phase reaction mechanism.

The lithium staging structure in partially delithiated Li_xFePO_4 nanowires ($x \approx 0.5$, $d = 65$ nm) was observed for the first time by an aberration-corrected ABF-STEM (Fig. 5).[53] Compared to pristine $LiFePO_4$ (Fig. 5(a)), the Li-extraction sites in half-charged $LiFePO_4$ are marked by orange circles (Fig. 5(c)). The lithium staging structure looks obvious, and the results are different from the previous models. Later, a single-phase transformation path was demonstrated to exist at very low overpotential during lithiated and dislithiated processes to yield a metastable staging-like atomic configuration in canonical Monte Caro simulations.[54] Meanwhile, the discovery of the metastable phase provided explanations regarding the high rate capability of $LiFePO_4$. In addition, the formation mechanism of the lithium staging structure and the factors influencing its formation were investigated. The atomic structure of partially chemically dislithiated 2% Nb-doped $LiFePO_4$ with particle size of ~ 200 nm was revealed by ABF imaging and the lithium staging structure was detected.[55] These studies showed that doping of Nb did not affect the formation of the lithium staging structure, indicating that the staging single phase was an intermediate or intrinsic metastable phase.

On the other hand, the lithium staging structure was used as "buffer" to relax volume expansion (about 6.8%) and facilitate the migration of Li ions. This supported the fact that the formation of the lithium staging structure is advantageous to the electrode kinetics. The phenomenon of staging $LiFePO_4$ with different sizes (70 nm and 50 nm) was detected by ABF imaging.[56] The ABF-STEM images of partially dislithiated 70 nm $LiFePO_4$ are shown in Fig. 6. The lithium staging structure mainly existed in the region between $LiFePO_4$and $FePO_4$, creating coexisting $LiFePO_4$/staging structure/$FePO_4$. Two $LiFePO_4$ samples with different sizes demonstrated the effect of size on the lithium staging region. In other words, the zone of the lithium staging structure becomes narrower as the $LiFePO_4$ size increases.

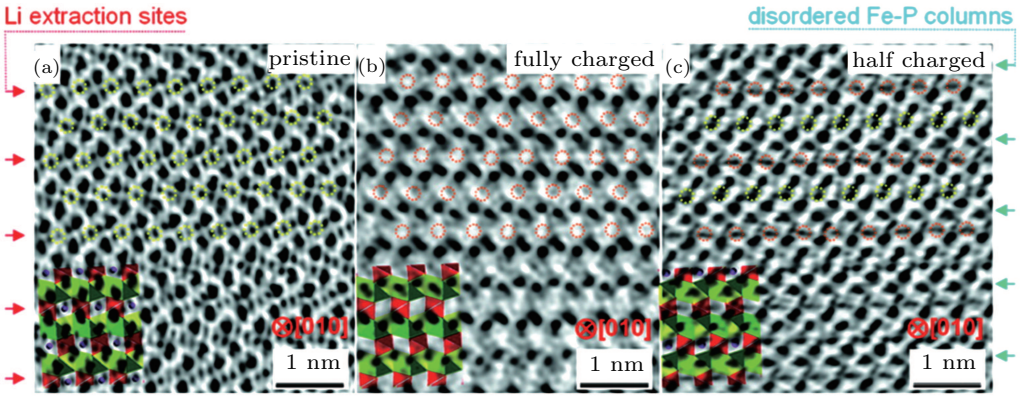


Fig. 5. (color online) ABF images showing Li ions of partially delithiated $LiFePO_4$ at every other row. (a) Pristine materials with the atomic structure of $LiFePO_4$ are shown as an inset, (b) fully charged state at atomic structure of $FePO_4$ shown for comparison, and (c) half-charged state depicting the Li staging structure. Note that Li sites are marked by yellow circles and delithiated sites are marked by orange circles.[53]

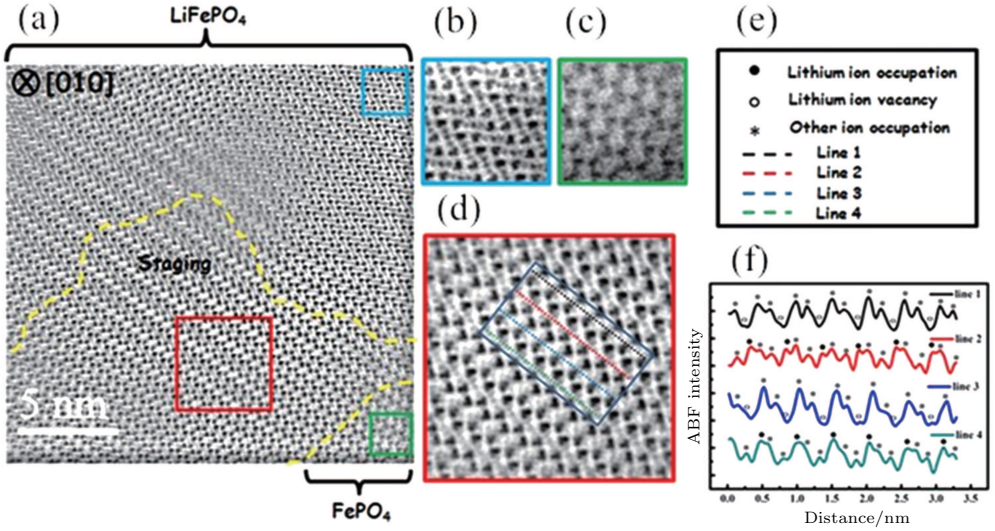


Fig. 6. (color online) (a) ABF image of 70 nm $LiFePO_4$ viewed at the [010] zone axis. The staging area is marked by dashed yellow lines. (b)–(d) Enlarged images of $LiFePO_4$, $FePO_4$ phase and interfacial phase with staging structure, corresponding to the tubes, green and red squares in (a), respectively. (e) and (f) The line profiles issued from the ABF image correspond to different colored lines in (d).[56]

The theoretical calculation regarding the formation of such staging structures was performed by density functional theory,[57] showing that the staging structure in partially delithiated $LiFePO_4$ is thermodynamically metastable but in the kinetically controlled state. A dual-interface model was also proposed and the results were consistent with experimentally observed three-phase coexisting $LiFePO_4$/staging structure/ $FePO_4$. The formation of the lithium staging structure was mainly ascribed to the Fe center mediating the interlayer Li–Li interaction, originating from the localized nature of Fe 3d electrons. The effective oxidation state of Fe redox depended on the configuration of the Li ions. Conversely, the diffusion of Li ions was influenced by the oxidation state of Fe but the size effect was not taken into consideration in this work. Overall, ABF imaging of STEM coupled with other characterization techniques would reveal the microscopic mechanism of structural evolution in $LiFePO_4$ in a step-by-step process.

4.2. Layered compounds $LiCoO_2$ and Li_2MnO_3

$LiCoO_2$ was first reported by Mizushima as a cathode material with high volumetric energy density.[58] $LiCoO_2$ cathode was employed in the first generation of commercial LIBs and still dominates the portable devices market. However, no more than 0.5 mole of Li ions can be extracted per mole of Co to maintain structural stability during electrochemical cycling, causing extremely low potential capacities of LIBs. Three kinds of layered structures of $LiCoO_2$ are O1-type, O2-type, and O3-type. The stacking sequences of O1, O2, and O3 are *ABAB*, *ABAC*, and *ABCABC*, respectively.[58–60] It has been observed that O2-Li_xCoO_2 can be formed in electrochemically cycled O3-$LiCoO_2$ electrodes via HAADF and ABF-STEM.[61] When $LiCoO_2$ cathodes are charged to 4.5 V ($x = 0.5$), the structure of $LiCoO_2$ should undergo a transformation from O3-type to O1-type (Fig. 7). In Figs. 7(b) and 7(c), the contrast of Co columns (pink line: ○) is obviously different from that of the black line (☆) acquired by the pristine $LiCoO_2$ ABF micrograph. The Co atoms are marked with Co1 and Co2, denoting different chemical environments of Co ion after delithiation at high voltage.

The different contrast of the Co atom is attributed to the interaction with the nearest Li ion and vacancy, providing information about the electron distribution and bond length distortion after Li ion extraction. In Fig. 7(d), the Li ion columns (Li1 and Li2) in the blue line (○) are also distinct from those in the black line (☆) from the pristine material, whose configuration is similar to the arrangement of the Li ion and vacancy in Fig. 7(a). Such configuration was observed along the (101) plane in the O1-$LiCoO_2$ lattice. As shown in Fig. 8, the phase transition that occurred during the first cycle was visible by HAADF-STEM. The phase transition from O3-$LiCoO_2$ to O1-$LiCoO_2$ was observed at $x = 0.5$ in nanosized Li_xCoO_2. This result does not agree well with the known phase diagram of Li_xCoO_2, where the O3 phase was kept before $x = 0.5$ and the initial formation of O1 occurred at $x = 0.3$.[62–64] Afterwards, the O2 phase started to form when the charge state was discharged to 3.0 V. The O2-type is metastable generally created by ionic exchange from $NaCoO_2$[59,60] and O3-type is a stable state. Earlier, it was thought that the phase transition processes of O2 and O3 were separate, meaning that they could not convert into each other once synthesized. This finding connected the two separated $LiCoO_2$ systems to each other, at least for nanoscale particles (50 nm) used experimentally.

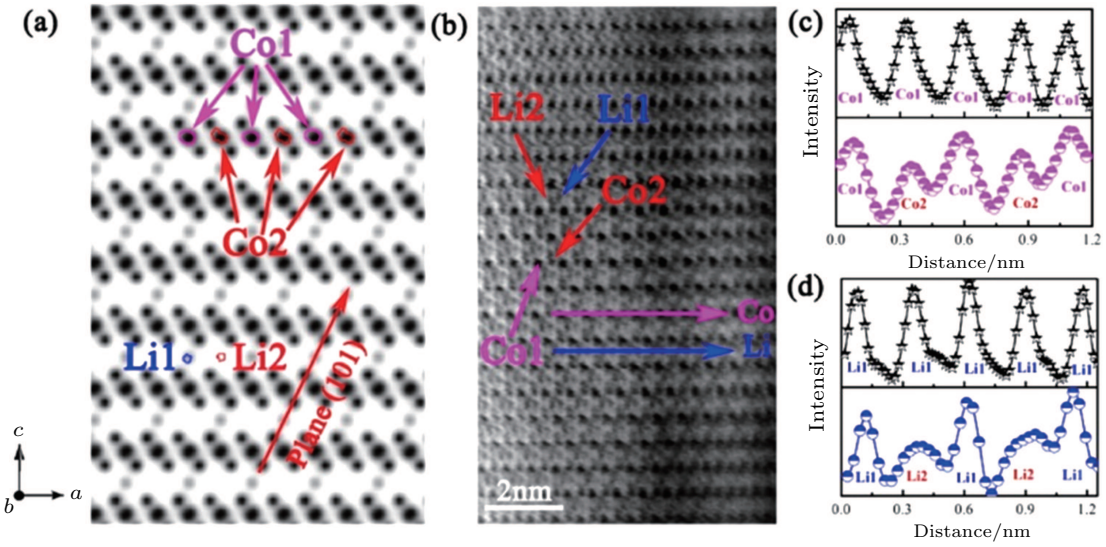


Fig. 7. (color online) (a) Simulated ABF micrograph of O1-type $Li_{0.5}CoO_2$ with ordered Li occupancies/vacancies arrangements at the [010] zone axis. (b) STEM ABF image of an $LiCoO_2$ electrode charged to 4.5 V at the [010] zone axis. The corresponding line profiles of (c) Co columns and (d) Li columns in the HAADF image, where the black line (☆) is acquired from the ABF micrograph of pristine $LiCoO_2$.[61]

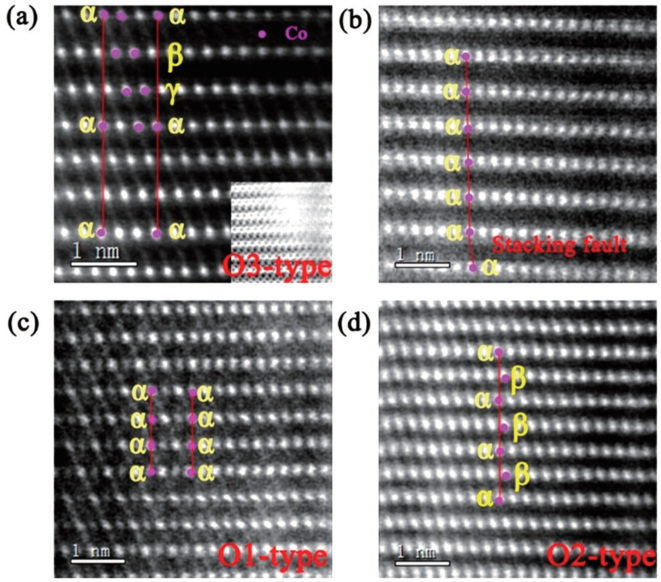


Fig. 8. (color online) HAADF image of surface structure: (a) pristine $LiCoO_2$, (b) $LiCoO_2$ charged to 4.2 V, (c) charged to 4.5 V, and (d) discharged to 3.0 V at the [010] zone axis.[61]

All-solid-state batteries equipped with solid-state electrolytes are effective approaches to address safety problems related to flammable organic liquid electrolytes. Solid-state electrolytes make it possible for lithium to be used in anodes and high voltage cathodes materials at the same time. The structure evolution of $LiCoO_2$ in all-solid-state LIB and structure at high voltage conditions have been experimentally studied *in situ* by STEM imaging.[65] The working all-solid-state LIB shown in Fig. 9(a) was designed, and electrochemical delithiation was directly observed at the atomic scale by employing a state-of-the-art chip by aberration-corrected STEM for the first time. The all-solid-state LIBs with gold anodes, $LiCoO_2$ cathodes, and Y and Ta-doped LLZO ($Li_{6.75}La_{2.84}Y_{0.16}Zr_{1.75}Ta_{0.25}O_{12}$) as the solid-state electrolyte (SSE) were built on micro-electro-mechanical system (MEMS) device nanochips using FIB milling.[66–68]

ABF and HAADF images of pristine $LiCoO_2$ cathodes are shown in Figs. 9(c) and 9(d), demonstrating the layered structures of $LiCoO_2$ cathodes. As shown in Fig. 10, after high voltage delithiation, the pristine single crystal $LiCoO_2$ became a nanosized polycrystal connected by coherent twin boundaries and antiphase domain boundaries. Figures 10(b)–10(e) also reveal that only two kinds of crystal orientations in the delithiated $LiCoO_2$ cathode existed and the original 109.5° coherent twin boundary in the pristine $LiCoO_2$ cathode increased to 112° due to the extraction of lithium ions. Contrasts in lithium layer in both HAADF and ABF micrographs are visible for both boundaries, suggesting that heavy atoms were present in the lithium layer. In this case, they concerned cobalt ions due to a phase transition in the layer structure, spinel and rock salt. Meanwhile, the layer spacing increased by 2.7% (±0.4%) due to the extraction of lithium ions and probably accumulated lithium or cobalt ions at the domain boundaries.[69–72]

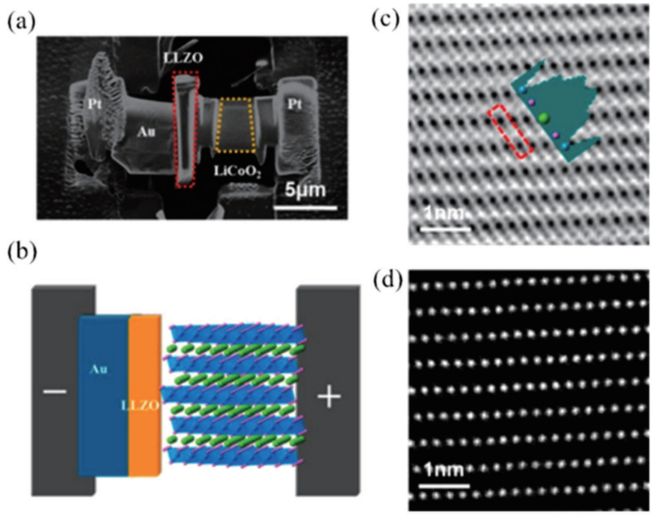


Fig. 9. (color online) (a) SEM image of an FIB fabricated battery on a nanochip in the applied electric field, and (b) corresponding schemes. The LLZO electrolyte and electron transparent area of the $LiCoO_2$ cathode are highlighted with a red dashed line and a yellow dashed line trapezoid in (a). (c) and (d) The pristine $LiCoO_2$ ABF with the corresponding line profile and HAADF micrographs acquired at the red dashed line rectangular zone shown in (c) with both lithium and oxygen contrasts. The green, purple, and cyan balls are lithium, oxygen, and cobalt ions, respectively.[65]

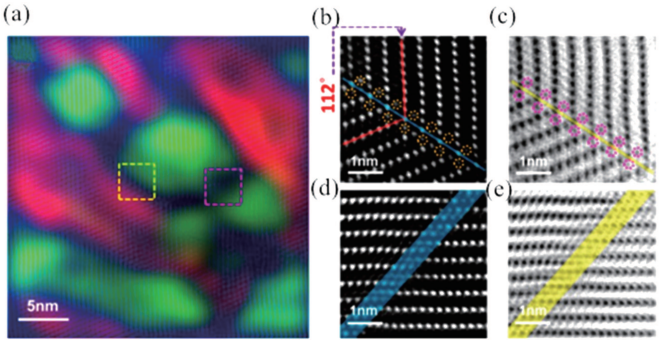


Fig. 10. (color online) (a) HAADF micrograph of a delithiated $LiCoO_2$ cathode colored using the GPA method. HAADF micrograph colored in blue, and two orientations colored in green and red. (b) and (d) Zoomed-in HAADF micrographs of the yellow, dashed-line, rectangular and pink areas, respectively. (c) and (e) Zoomed-in ABF micrographs of the yellow, dashed-line, rectangular and pink areas, respectively.[65]

To elucidate the formation of both boundaries, three models with different lithium concentrations were utilized to calculate the formation energies. The interface energies of coherent twin boundaries and antiphase domain boundaries with different Li concentrations suggested that the antiphase domain boundary is less likely to form than the coherent twin boundary during the delithiation process, which is consistent with the HAADF micrographs. Thus, this work not only boosted the development of all-solid-state batteries but also introduced the state-of-the-art chip to study electrochemical processes. Furthermore, the results of the electrochemical measurements will be improved due to the decreased contact resistances.

Apart from $LiCoO_2$, a kind of compounded material composed of Li_2MnO_3 and $LiMO_2$ (M = Mn, Ni, Co, Fe, Cr, etc.) layers were reported and identified as $xLiMO_2 \cdot (1-x)Li_2MnO_3$ or Li-rich layered materials. LIBs with these cathode materials can provide much higher energy densities than those with $LiCoO_2$.[73,74] Li_2MnO_3 is considered as the end member of the $xLiMO_2 \cdot (1-x)Li_2MnO_3$ compound family, extensively investigated for applications as cathodes in LIBs.[74–76] The structure of Li_2MnO_3 is a layered $Li[Li_{1/3}Mn_{2/3}]O_2$ structure, where Li^+ and Mn^{4+} ions occupy the octahedral interstices of the cubic closely-packed oxygen lattice. Because the content of Li^+ is rich, they are thus called Li-rich layered materials. However, delithiation is difficult in Li_2MnO_3, leading to much lower experimental capacities than the theoretical values.[77,78] Some studies reported the observation of crystal structure transformation of Li_2MnO_3 implemented by the aberration-corrected STEM and high-resolution XRD, revealing the coexistence of monoclinic spinel and rock salt structures.[79] Hence, localized and inhomogeneous structural evolution was discovered.

The transition metal atoms occupying the Li plane is obvious, and considered as a key step in generating the rock salt or spinel structure. Many small regions marked by strain are surrounded by darker contrast. Meanwhile, the Li_2MnO_3 regions are adjacent to the transferred regions, pointing to the inhomogeneous nature of structure evolution. High-resolution XRD showed that electrochemical reaction occurred in most particles because Li_2MnO_3 regions and transferred regions existed in most particles of surface and away from the surface towards the bulk. The result is different from previous conclusions that the electrochemical reactions were confined at the surface in similar layered oxide materials.[80–82] EELS analysis provided solid information regarding valence of elements and their chemical environments. In conclusion, the following transformation sequence was proposed: $Li_2MnO_3 \rightarrow Li_xMn_{4/3}O_4 \rightarrow Li_xMn_2O_4 \rightarrow Mn_3O_4 \rightarrow MnO$. Oxygen trapping appeared inside the particles, producing Mn-deficient topotaxial $Li_xMn_2O_4$ regions. However, O diffusion at the surface of the particles was easier, leading to the formation of MnO. Finally, the observed capacity fading may be attributed to a phase transition.

Inferior rate capacity and voltage decay of Li-rich layered materials during electrochemical cycle are great obstacles in practical applications.[74] These issues are attributed to poor electrode kinetics, where kinetics of Li-rich layered material could even be worse with largely dense particles. Because the Li_2MnO_3 phase is partially linked to electrochemical activation, several cycles are essential to achieving full activation. Such an electrochemical cycle is harmful to reversible capacity.[83,84] Therefore, tremendous efforts have been made to solve these issues, including by surface coating with Al_2O_3, $AlPO_4$, AlF_3[85,86] and nanosizing,[87,88] which can improve the behaviors of the cathode to some degree.

Some studies demonstrated that the electrochemical activity could be facilitated by structural defects.[84,89,90] Gradient surface Na^+ doping achieved by calcination process of Li-rich layered material in a molten NaCl state was thus introduced to enhance the kinetics of Li-rich layered materials.[91] The structure with gradient surface Na^+ is shown schematically in Fig. 11. The HAADF image corresponding to the ABF view and ABF profile of Li-rich layered material with gradient surface Na^+ doping is presented in Fig. 12. It can be seen from Fig. 12(a) that there is no cation mixture of Li ions and transition metal (TM) ions, because there is no visible contrast in the Li slab. The contrast in the Li slab of ABF induced by TM ions can be excluded. The atomic number of Na was larger than that of Li. The visible contrast in the Li slab of ABF was generated by an increscent averaged atom number. The higher peak of the ABF line profile also indicated the existence of Na^+ in the Li slab. All these data observed using aberration-corrected STEM confirmed that doped Na^+ occupied the Li sites.

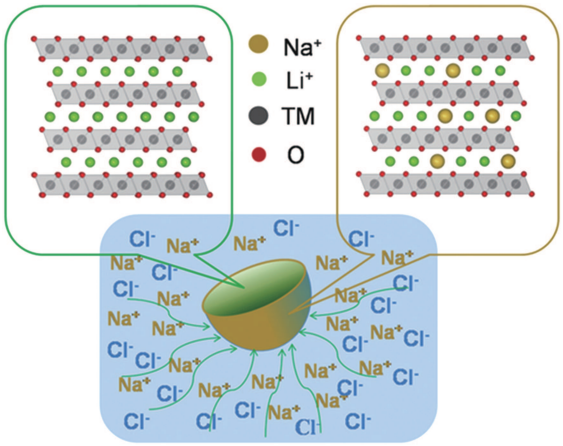


Fig. 11. (color online) Schematic illustration of the structural design of gradient surface Na^+ doped Li-rich material.[91]

The pinning effects provoked by gradient Na^+ doping can stabilize the layered structure by abounding the structural defects. Moreover, this could enlarge the layer-spacing of (003) and (104), as confirmed by XRD. The latter might speed up the diffusion of Li ions in the layered structure. The electrochemical characterizations suggested that when compared with pristine Li_2MnO_3, the reversible capacity and cyclic stability of Li_2MnO_3 cathode with gradient surface Na^+ doping were highly improved. Doping foreign ions on the surface of electrode materials is, thus, a feasible way to improve electrode kinetics and stabilize the surficial structure. To further advance batteries, the determination of electrochemical mechanism would be crucial to optimize electrode performances.

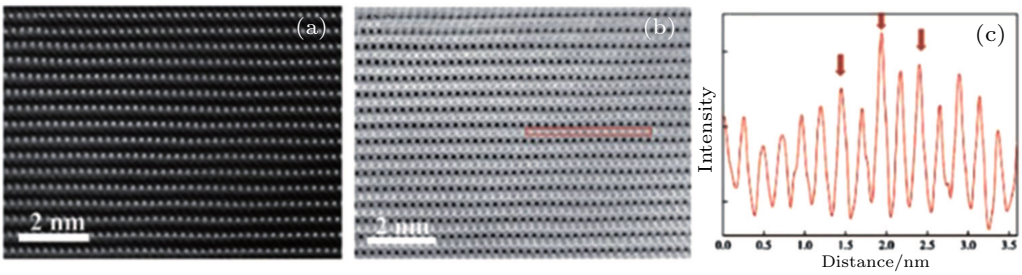


Fig. 12. (color online) STEM of gradient surface Na^{+} doped Li-rich material surface along [010] zone axis: (a) HAADF image, (b) ABF image, and (c) ABF line profile.[91]

4.3. Spinel compound $LiMn_2O_4$

Spinel $LiMn_2O_4$ and its derivatives are excellent cathode materials for LIBs due to their high energy densities, low cost, and favorable safety.[92–96] However, the main problem with $LiMn_2O_4$ is the serious capacity fading during electrochemical cycling or lengthy storage time, especially at elevated temperatures.[97–100] To overcome these issues, several theories were put forward to explain the phenomena, including electrochemical reaction with electrolytes at high voltage,[101] instability of the two-phase structure at charge state,[102,103] phase transformation from cubic spinel to tetragonal rock-salt structure due to nonequilibrium lithiation,[104] and manganese dissolution.[102,105,106] Even though the structure of $LiMn_2O_4$ is relatively stable, migration of Mn ions from octahedral sites to lithium tetrahedral sites in few nanometers surface region during cycling could generate $LiMn_3O_4$-like defect-spinel structures.[107,108] The structure distortion at the surface is related to manganese dissolution. Thus, the precise structural evolution in the surface region would be vital in exploring the cause of capacity fading and measures to improve the cycling performance of $LiMn_2O_4$ cathodes.

It was reported that an unusual spinel-to-layered transformation of the $LiMn_2O_4$ cathode was observed by aberration-corrector STEM, and possible transformation processes were given.[109] Moreover, an atomic-level surface $LiMn_2O_4$ cathode subjected to heat-treatment in various atmospheres showed similar transformations.[109] A $LiMn_2O_4$ cathode immersed in half-cell was cycled between 3 V and 4.5 V (normal voltage) for six cycles to stabilize, then cycled between 3 V and 4.9 V (high voltage) for ten cycles. The subsequent cycles were implemented between 3 V and 4.5 V. After 100 cycles, no newly formed phases were observed by XRD, and the lattice parameters of $LiMn_2O_4$ cathode became smaller than those of pristine materials. This was partially induced by the loss of Mn ions. The XRD results revealed that the spinel structure of $LiMn_2O_4$ cathode was relatively stable. Hence, the degradation of cycling performance was probably connected to the local structure of the surface.

The HADDF images of sub-surface and surface of $LiMn_2O_4$ cathode cycled in normal voltage window are shown in Fig. 13. The subsurface still maintained the spinel structure, which can be seen from Figs. 13(a) and 13(b) and confirmed by line profile of Figs. 13(e_1) and 13(f_1). The migration of Mn ions from Mn octahedral sites to lithium tetrahedral sites induced surface distortion, forming defect $LiMn_3O_4$-like structures. Compared with ideal $LiMn_3O_4$ stimulated structure and line profiles, it was demonstrated that the surface structure is intermediate stage of structure evolution from spinel $LiMn_2O_4$ to defect spinel $LiMn_3O_4$. As illustrated in Fig. 14, the structure of the bulk kept the standard spinel, and both the distorted surface and subsurface regions after high voltage cycling were larger than those obtained after normal voltage cycling. An unusual layered structure in the surface region appears in Fig. 14(c). The spacing between layers was estimated to be about 4.7 Å, which is comparable to that of many-layered cathode materials.[61,110] During high voltage cycling, Mn ions of the surface $LiMn_3O_4$-like structure region from the Mn tetrahedral sites and Mn octahedral sites in some regions fully occupy Mn octahedral sites in other regions nearby, forming a Mn-deficient $LiMn_3O_4$-like structure and fresh layered-like structure.

The surface electronic structures of the $LiMn_2O_4$ cathode at different electrochemical states were studied by x-ray photoelectron spectroscopy. The existence of Mn^{3+} on the surface region indicated that oxygen loss may occur on the surface of the $LiMn_2O_4$ cathode to reduce Mn^{4+} ions into Mn^{3+} compensating charges. During this process, more oxygen may be lost at high cycling voltages. The unusual structure transformation caused by Mn ion migration was related to the reduction of Mn^{4+} and oxygen loss, confirmed by heat-treatment experiments of the $LiMn_2O_4$ cathode. Mn^{3+} played a key role in the kinetics of the unusual structure transformation in spinel $LiMn_2O_4$ cathodes, and the particular atmosphere could control the surface oxygen loss so that the structural transformation could clearly be reconstructed. The unusual spinel-to-layered transformation on the surface of $LiMn_2O_4$ cathodes

may be a major factor accounting for the degradation of the cycling performance. Some measures can be taken to stabilize the surficial structure to enhance the properties of spinel $LiMn_2O_4$ cathodes.

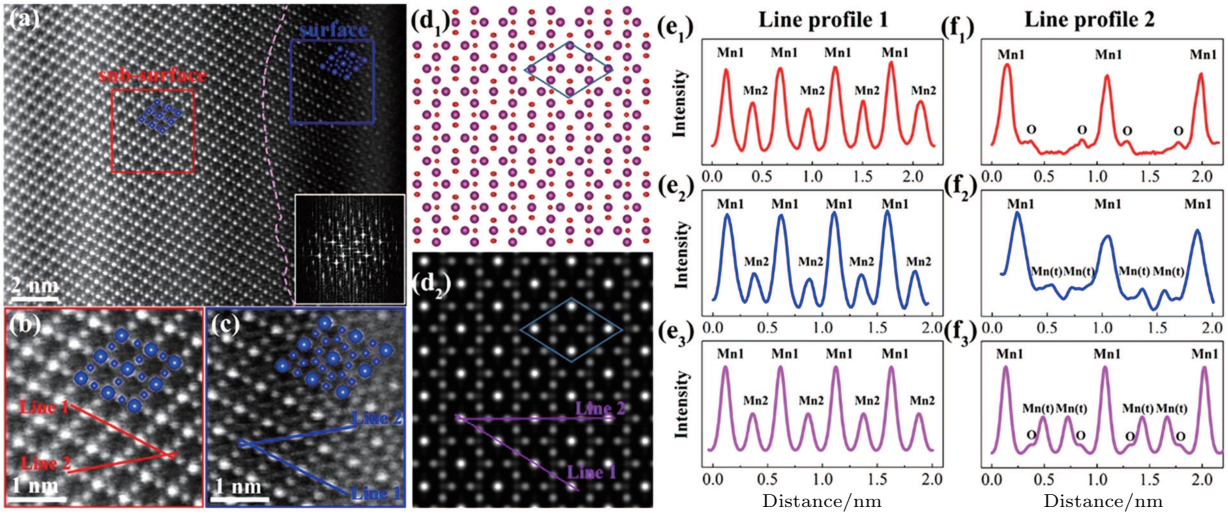


Fig. 13. (color online) (a) HAADF image of $LiMn_2O_4$ after normal voltage cycling. (b) and (c) Enlarged images of the surface and subsurface regions, corresponding respectively to the red and blue boxes shown in panel (a). (d_1) Crystal structure of defect-spinel $LiMn_3O_4$ viewed along the[110] direction. The Mn atoms (purple) occupy both octahedral and tetrahedral sites and O atoms are depicted in red. (d_2) Simulated HAADF image. (e) and (f) Line profiles corresponding to the red lines in panel (b), blue lines in panel (c), and purple lines in (d_2), respectively.[109]

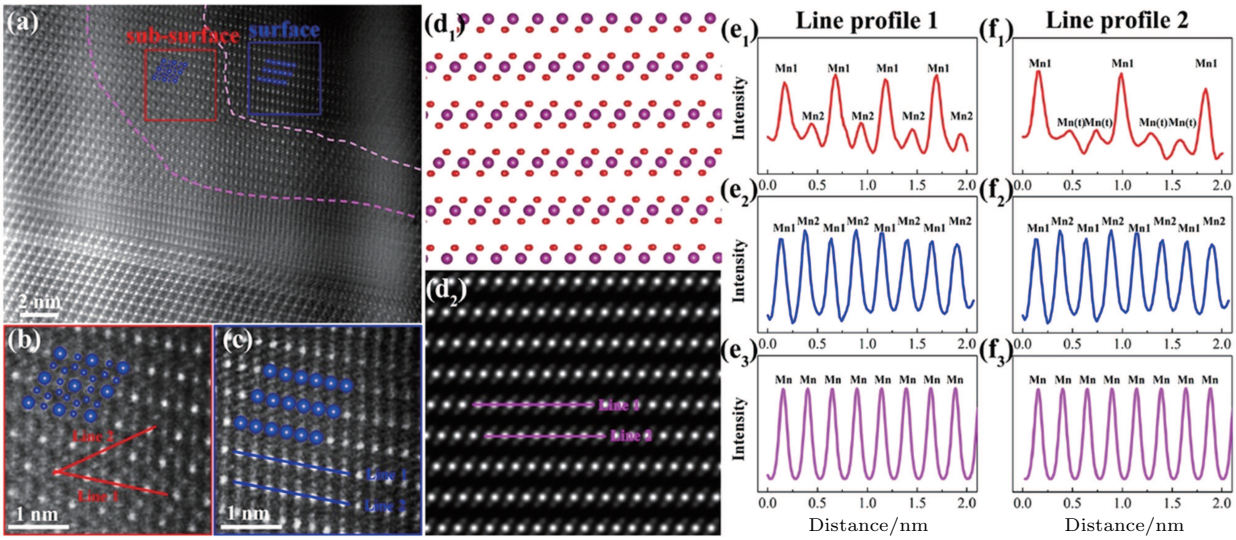


Fig. 14. (color online) HAADF image of $LiMn_2O_4$ after high voltage cycling. (b) and (c) Enlarged images of the surface and subsurface regions, Corresponding, respectively, to the red and blue boxes in panel (a). (d_1) Crystal structure of the layered viewed along the [100] direction. Mn atoms (purple) occupy octahedral sites and O atoms are depicted in red. (d_2) Simulated HAADF image. (e) and (f) Line profiles corresponding to the red lines in panel (b), blue lines in panel (c), and black lines in panel (d), respectively.[109]

5. Perspectives

This review is mainly focused on applications of HAADF and ABF of STEM in the characterization of cathode materials of LIBs. For decades, the research and development dealing with LIBs have been focused on rechargeable features. However, little attention was devoted to detecting the mechanisms involved in the redox processes, mainly due to difficulties in locating the Li ions. Li ions play crucial roles in energy storage and transfer in LIBs. The advantage of ABF imaging is visualizing the Li ions, thereby promoting the development of LIBs. Using ABF imaging, many electrochemical reaction mechanisms were revealed and design guidance was outlined to improve the properties of LIBs to meet the increasing demands of clean energy and environmental protection. All-solid-state batteries attracted more attention in terms of high energy density and outstanding safety. However, many problems emerged due to the use of solid electrolytes, including new electrochemical reaction mechanisms, unknown transitional phases formed by diffusion between two solid states and increased contact resistance. The ion diffusion of solid electrolytes is considered as a key factor to determine the kinetics of electrochemical processes.[111] It is reported that ABF and EELS

can gain great insight into the solid ion conductor.[112] The increased resistance of all-solid-state batteries was attributed to the surface and interface atomic-level structures revealed by HAADF and ABF in the aberration-corrected STEM.

Aberration-corrected STEM can quickly identify the fundamental chemical and physical causes of problems and figure out feasible ways to solve them. Nowadays, the HAADF and ABF imaging techniques of STEM become powerful in characterizing atomic-level structures of various kinds of materials, which is vital for optimizing the properties of materials and creating new materials. Considering the powerful capability of *in situ* investigation, *in situ* STEM has been a focus of the development of STEM. It can provide observation in real time during reaction processes and possibly identify the reaction mechanism. With the development of *in situ* holders of the STEM, various reactions under different conditions can be implemented in STEM, including heating, cooling and voltage application. However, the interaction between high-energy electron beams and the specimen could also yield undesired electron beam damage to the specimen. To minimize this effect, shorter acquisition time to lower dose and utilization of an accelerating voltage below threshold have been put forward and demonstrated to be effective.[113,114] Finally, a combination of STEM with other probing techniques, including electron energy-loss spectroscopy (EELS) and energy dispersive spectroscopy (EDS), would offer more comprehensive information about various materials. STEM is expected to make more contributions in many fields.

References

[1] Scherzer O 1949 *J. Appl. Phys.* **20** 20
[2] Haider M, Uhlemann S, Schwan E, Rose H, Kabius B and Urban K 1998 *Nature* **392** 768
[3] Haider M, Rose H, Uhlemann S, Schwan E, Kabius B and Urban K 1998 *Ultramicroscopy* **75** 53
[4] O'Keefe M A, Hetherington C J D, Wang Y C, Nelson E C, Turner J H, Kisielowski C, Malm J O, Mueller R, Ringnalda J, Pan M and Thust A 2001 *Ultramicroscopy* **89** 215
[5] Tiemeijer P C, Bischoff M, Freitag B and Kisielowski C 2012 *Ultramicroscopy* **114** 72
[6] Erni R, Rossell M D, Kisielowski C and Dahmen U 2009 *Phys. Rev. Lett.* **102** 096101
[7] Cheng S, Lü H, Shi Z and Cui J 2012 *Acta Phys. Sin.* **61** 126201 (in Chinese)
[8] Lai Y 2010 *Acta Phys. Sin.* **59** 8814 (in Chinese)
[9] Pennycook S J and Boatner L A 1988 *Nature* **336** 565
[10] Hillyard S and Silcox J 1995 *Ultramicroscopy* **58** 6
[11] Okunishi E, Ishikawa I, Sawada H, Hosokawa F, Hori M and Kondo Y 2009 *Microsc. Microanal.* **15** 164
[12] Findlay S D, Shibata N, Sawada H, Okunishi E, Kono Y, Yamamoto T and Ikuhara Y 2009 *Appl. Phys. Lett.* **95** 191913
[13] Findlay S D, Shibata N, Sawada H, Okunishi E, Kono Y and Ikuhara Y 2010 *Ultramicroscopy* **110** 903
[14] Okunishi E, Sawada H and Kondo Y 2012 *Micro* **43** 538
[15] Findlay S D, Azuma S, Shibata N, Okunishi E and Ikuhara Y 2011 *Ultramicroscopy* **111** 285
[16] Findlay S D, Lugg N R, Shibata N, Allen L J and Ikuhara Y 2011 *Ultramicroscopy* **111** 1144
[17] Findlay S D, Huang R, Ishikawa R, Shibata N and Ikuhara Y 2017 *Microscopy* **66** 3
[18] Mathews M M 1953 *Transactions of the American Microscopical Society* **72** 190
[19] Hanssen K J and Trepte L 1971 *Optik* **33** 166 (in German)
Hanssen K J and Trepte L 1971 *Optik* **33** 166
[20] Rose H 1976 *Ultramicroscopy* **2** 251
[21] Komoda T 1966 *Jpn. J. Appl. Phys.* **5** 603
[22] Cowley J M 1969 *Appl. Phys. Lett.* **15** 58
[23] Cowley J M, Hansen M S and Wang S Y 1995 *Ultramicroscopy* **58** 18
[24] Ishikawa R, Okunishi E, Sawada H, Kondo Y, Hosokawa F and Abe E 2011 *Nat. Mater.* **10** 278
[25] Anstis G R, Cai D Q and Cockayne D J H 2003 *Ultramicroscopy* **94** 309
[26] Okunishi E, Sawada H and Kondo Y 2012 *Micro* **43** 538
[27] Tarascon J M and Armand M 2001 *Nature* **414** 359
[28] Thackeray M M, Wolverton C and Iasscs E D 2012 *Energy Environ. Sci.* **5** 7854
[29] Dunn B, Kamath H and Tarascon J M 2011 *Science* **334** 928
[30] Senga R and Suenaga K 2015 *Nat. Commun.* **6** 7943
[31] Huang R, Ikuhara Y H, Mizoguchi T, Findlay S D, Kuwabara A, Fisher C A J, Moriwake H, Oki H, Hirayama T and Ikuhara Y 2011 *Angewandte Chemie-Int. Ed.* **50** 3053
[32] Huang R, Hitosugi T, Findlay S D, Fisher C A J, Ikuhara Y H, Moriwake H, Oki, H and Ikuhara Y 2011 *Appl. Phys. Lett.* **98** 051913
[33] Padhi A K, Nanjundaswamy K S and Goodenough J B 1997 *J. Electrochem. Sci.* **144** 1188
[34] Delacourt C, Laffont L, Bouchet R, Wurm C, Leriche J B, Morcette M, Tarascon J M and Masquelier C 2005 *J. Electrochem. Soc.* **152** A913
[35] Yonemura M, Yamada A, Takei Y, Sonoyama N and Kanno R 2004 *J. Electrochem. Soc.* **151** A1352
[36] Molenda J, Ojczyk W, Swierczek K, Zajac W, Krok F, Dygas J and Liu R S 2006 *Solid State Ionics* **177** 2617
[37] Prosini P P, Lisi M, Zane D and Pasquali M 2002 *Solid State Ionics* **148** 45
[38] Amin R, Balaya P and Maier J 2007 *Electrochem. Solid State Lett.* **10** A13
[39] Amin R and Maier J 2008 *Solid State Ionics* **178** 1831
[40] Amin R, Lin C T and Maier J 2008 *Phys. Chem. Chem. Phys.* **10** 3519
[41] Yang S F, Zavalij P Y and Whittingham M S 2001 *Electrochem. Commun.* **3** 505
[42] Yang S F, Song Y N, Zavalij P Y and Stanley Whittingham M 2002 *Electrochem. Commun.* **4** 239
[43] Delacourt C, Poizot P, Levasseur S and Masquelier C 2006 *Electrochem. Solid State Lett.* **9** A352
[44] Bakenov Z and Taniguchi I 2010 *Electrochem. Commun.* **12** 75
[45] Huang H, Yin S C and Nazar L F 2001 *Electrochem. Solid State Lett.* **4** A170
[46] Chen Z and Dahn J R 2002 *J. Eletrochem. Soc.* **149** A1184
[47] Dominko R, Bele M, Gaberscek M, Remskar M, Hanzel D and Jamnik J 2005 *J. Eletrochem. Soc.* **152** A858
[48] Gaberscek M, Dominko R, Bele M, Remskar M, Hanzel D and Jamnik J 2005 *Solid State Ionics* **176** 1801
[49] Srinivasan V and Newman J 2004 *J. Electrochem. Sci.* **151** A1517
[50] Andersson A S and Thomas J O 2001 *J. Power Sources* **97–98** 498
[51] Laffont L, Delacout C, Gibt P, Wu M Y, Kooyman P, Masquelier C and Tarascon J M 2006 *Chem. Mater.* **18** 5520
[52] Delmas C, Maccario M, Croguennec L, Le Cras F and Weil F 2008 *Nat. Mater.* **7** 665
[53] Gu L, Zhu C B, Li H, Yu Y, Li C L, Tsukimoto S, Maier J and Ikuhara Y 2011 *J. Am. Chem. Soc.* **133** 4661
[54] Malik R, Zhou F and Ceder G 2011 *Nat. Mater.* **10** 587
[55] Suo L, Han W, Lu X, Gu L, Hu Y S, Li H, Chen D, Chen L, Tsukimoto S and Ikuhara Y 2012 *Phys. Chem. Chem. Phys.* **14** 5363
[56] Zhu C B, Gu L, Suo L, Popovic J, Li H, Ikuhara Y and Maier J 2014 *Adv. Funct. Mater.* **24** 312
[57] Sun Y, Lu X, Xiao R J, Li H and Huang X J 2012 *Chem. Mater.* **24** 4693
[58] Mizushima K, JonesP C, Wiseman P J and Goodenough J B 1980 *Mater. Res. Bull.* **15** 783
[59] Delmas C, Braconnier J J and Hagenmuller P 1982 *Mater. Res. Bull.* **17** 117

[60] Carlier D, Saadoune I, Croguennec L, Menetrier M, Suard E and Delmas C 2001 *Solid State Ionics* **144** 263
[61] Lu X, Sun Y, Jian Z, He X, Gu L, Hu Y S, Li H, Wang Z, Chen W, Duan X, Chen L, Maier J, Tsukimoto S and Ikuhara Y 2012 *Nano Lett.* **12** 6192
[62] Van der Ven A, Aydinol M K, Ceder G, Kresse G and Hafner J 1998 *Phys. Rev. B* **58** 2975
[63] Amatucci G G, Tarascon J M and Klein L C 1996 *J. Electrochem. Soc.* **143** 1114
[64] Liu L J, Chen L Q, Huang X J, Yang X Q, Yoon W S, Lee H S and McBreen J 2004 *J. Electrochem. Soc.* **151** A1344
[65] Gong Y, Zhang J N, Jiang L W, Shi J A, Zhang Q H, Yang Z Z, Zou D L, Wang J Y, Yu X Q, Xiao R J, Hu Y S, Gu L, Li H and and Chen L Q 2017 *J. Am. Chem. Soc.* **139** 4274
[66] Murugan R, Thangadurai V and Weppner W 2007 *Angew. Chem. Int. Ed.* **46** 7778
[67] Li Y, Cao Y and Guo X 2013 *Solid State Ionics* **253** 76
[68] Li Y, Wang Z, Li C, Cao Y and Guo X 2014 *J. Power Sources* **248** 642
[69] Hou P Y, Chu G, Gao J, Zhang Y T and Zhang L Q 2016 *Chin. Phys. B* **25** 016104
[70] Reimers J N and Dahn J R 1992 *J. Electrochem. Soc.* **139** 2091
[71] Amatucci G G, Tarascon J M and Klein L C 1996 *J. Electrochem. Soc.* **143** 1114
[72] Okubo M, Hosono E, Kim J, Enomoto M, Kojima N, Kudo, T, Zhou H and Honma I 2007 *J. Am. Chem. Soc.* **129** 7444
[73] Thackeray M M, Johnson C S, Vaughey J T, Li N and Hackney S A 2005 *J. Mater. Chem.* **15** 2257
[74] Thackeray M M, Kang S H, Johnson C S, Vaughey J T, Benedek R and Hackney S A 2007 *J. Mater. Chem.* **30** 3112
[75] Trask S E, Li Y, Kubal J J, Bettge M, Polzin B J, Zhu Y, Jansen A N and Abraham D P 2014 *J. Power Sources* **259** 233
[76] Li Y, Bettge M, Polzin B, Zhu Y, Balasubramanian M and Abraham D P 2013 *J. Electrochem. Soc.* **160** A3006
[77] Croy J R, Park J S, Dogan F, Johnson C S, Key B and Balasubramanian M 2014 *Chem. Mater.* **26** 7091
[78] Wang R, He X Q, He L H, Wang F W, Xiao R J, Gu L, Li H and Chen L Q 2013 *Adv. Energy Mater.* **3** 1358
[79] Phillips P J, Bareno J, Li Y, Abraham D P and Klie R F 2015 *Adv. Energy Mater.* **5** 1501252
[80] Yan P F, Xiao L, Zheng J M, Zhou Y G, He Y, Zu X T, Mao S X, Xiao J, Gao F, Zhang J G and Wang C M 2015 *Chem. Mater.* **27** 975
[81] Zheng J M, Gu M, Xiao J, Zuo P J, Wang C M and Zhang J G 2013 *Nano Lett.* **13** 3824
[82] Boulineau A, Simonin L, Colin J F, Bourbon C and Patoux S 2013 *Nano Lett.* **13** 3857
[83] Oh P, Myeong S, Cho W, Lee M J, Ko M, Jeong H Y and Cho J 2014 *Nano Lett.* **14** 5965
[84] Yu D Y W, Yanagida K, Kato Y and Nakamura H 2009 *J. Electrochem. Soc.* **156** A417
[85] Cho J, Kim T G, Kim C J, Lee J G, Kim Y W and Park B 2005 *J. Power Sources* **146** 58
[86] Rosina K J, Jiang M, Zeng D, Salager E, Best A S and Grey C P 2012 *J. Mater. Chem.* **22** 20602
[87] Yu X, Lyu Y, Gu L, Wu H, Bak S M, Zhou Y, Amine K, Ehrlich S N, Li H, Nam K W and Yang Y Q 2014 *Adv. Energy Mater.* **4** 1300950
[88] Wei G Z, Lu X, Ke F S, Huang L, Li J T, Wang Z X, Zhou Z Y and Sun S G 2010 *Adv. Mater.* **22** 4364
[89] Kang S H, Johnson C S, Vaughey J T, Amine K and Thackeray M M 2006 *J. Electrochem. Soc.* **153** A1186
[90] Boulineau A, Croguennec L, Delmas C and Weil F 2010 *Solid State Ionics* **180** 1652
[91] Qin R P, Shi J L, Xiao D D, Zhang X D, Yu Y X, Zhao Y B, Gu L and Guo Y G 2016 *Adv. Energy Mater.* **6** 1501914
[92] Tarascon J M, Wang E, Shokoohi F K, McKinnon W R and Colson S 1991 *J. Electrochem. Soc.* **138** 2859
[93] Tarascon J M, McKinnon W R, Coowar F, Bowmer T N, Amatucci G and Guyomard D 1994 *J. Electrochem. Soc.* **141** 1421
[94] Liu J and Manthiram A 2009 *Chem. Mater.* **21** 1695
[95] Kim J H, Myung S T, Yoon C S, Kang S G and Sun Y K 2004 *Chem. Mater.* **16** 906
[96] Cabana J, Casas-Cabanas M, Omenya F O, Chernova N A, Zeng D, Whittingham M S and Grey C P 2012 *Chem. Mater.* **24** 2952
[97] Park S B, Shin H C, Lee W G, Cho W I and Jang H 2008 *J. Power Sources* **180** 597
[98] Dai Y, Cai L and White R E 2013 *J. Electrochem. Soc.* **160** A182
[99] Yoon T, Park S, Mun J, Ryu J H, Choi W, Kang Y S, Park J H and Oh S M 2012 *J. Power Sources* **215** 312
[100] Manthiram A, Chemelewski K and Lee E S 2014 *Energy Environ. Sci.* **7** 1339
[101] Pistoia G, Antonini A, Rosati R and Zane D 1996 *Electrochim. Acta* **41** 2683
[102] Jang D H, Shin Y J and Oh S M 1996 *J. Electrochem. Soc.* **143** 2204
[103] Xia Y Y, Zhou Y H and Yoshio M 1997 *J. Electrochem. Soc.* **144** 2593
[104] Thackeray M M, Shao-Horn Y, Kahaian A J, Kepler K D, Vaughey J T and Hackney S A 1999 *Electrochem. Solid-State Lett.* **1** 7
[105] Zhan C, Lu J, Jeremy Kropf A, Wu T P, Jansen A N, Sun Y K, Qiu X P and Amine K 2013 *Nat. Commun.* **4** 2437
[106] Aurbacha D, Levia M D, Gamulskia K, Markovskya B, Salitra G, Levia E, Heiderb U, Heiderb L and Oestenb R 1999 *J. Power Sources* **81–82** 472
[107] Tang D C, Sun Y, Yang Z Z, Ben L B, Gu L and Huang X J 2014 *Chem. Mater.* **26** 3535
[108] Li M X, Ben L B, Sun Y, Wang H, Yang Z Z, Gu L, Yu X Q, Yang X Q, Zhao H F, Yu R, Armand M and Huang X J 2015 *Chem. Mater.* **27** 292
[109] Ben L B, Yu H L, Chen B, Chen Y Y, Gong Y, Yang X N, Gu L and Huang X J 2017 *Appl. Mater. Interfaces* **9** 35463
[110] Yan P F, Zheng J M, Lv D P, Wei Y, Zheng J X, Wang Z G, Kuppan S, Yu J G, Luo L L, Edwards D, Olszta M, Amine K, Liu J, Xiao J, Pan F, Chen G Y, Zhang J G and Wang C M 2015 *Chem. Mater.* **27** 5393
[111] Kato Y, Hori S, Saito T, Suzuki K, Hirayama M, Mitsui A, Yonemura M, Iba H and Kanno R 2016 *Nat. Energ.* **1** 16030
[112] Gao X, Fisher C A J, Kimura T, Ikuhara Y H, Moriwake H, Kuwabara A, Oki H, Tojigamori T, Huang R and Ikuhara Y 2013 *Chem. Mater.* **25** 1607
[113] Lin F, Markus I M, Doeff M M and Xin L H 2015 *Sci. Rep.* **4** 5694
[114] Krivanek O L, Chisholm M F, Nicolosi V, Pennycook T J, Corbin G J, Dellby N, Murfitt M F, Own C S, Szilagyi Z S, Oxley M P, Pantelides S T and Pennycook S J 2010 *Nature* **464** 571